Check for updates

Iridium-(κ²-NSi) catalyzed dehydrogenation of formic acid: effect of auxiliary ligands on the catalytic performance†

Alejandra Gomez-España,[a,b] Jorge L. Lopez-Morales, [ID] [a] Belinda Español-Sanchez,[a] Pilar García-Orduña, [ID] [a] Fernando J. Lahoz, [ID] [a] Manuel Iglesias [ID] [a] and Francisco J. Fernández-Alvarez [ID] *[a]

The iridium(III) complexes [Ir(H)(Cl)(κ²-NSi^{tBu_2})(κ²-bipy^{Me_2})] (**2**) and [Ir(H)(OTf)(κ²-NSi^{tBu_2})(κ²-bipy^{Me_2})] (**3**) (NSi^{tBu_2} = {4-methylpyridine-2-yloxy}ditertbutylsilyl) have been synthesized and characterized including X-ray studies of **3**. A comparative study of the catalytic activity of complexes **2**, **3**, [Ir(H)(OTf)(κ²-NSi^{tBu_2})(coe)] (**4**), and [Ir(H)(OTf)(κ²-NSi^{tBu_2})(PCy$_3$)] (**5**) (0.1 mol%) as catalysts precursors for the solventless formic acid dehydrogenation (FADH) in the presence of Et$_3$N (40 mol%) at 353 K has been performed. The highest activity (TOF$_{5\ min}$ ≈ 3260 h^{-1}) has been obtained with **3** at 373 K. However, at that temperature the FTIR spectra show traces of CO together with the desired products (H$_2$ and CO$_2$). Thus, the best performance was achieved at 353 K (TOF$_{5\ min}$ ≈ 1210 h^{-1} and no observable CO). Kinetic studies at variable temperature show that the activation energy of the **3**-catalyzed FADH process is 16.76 kcal mol^{-1}. Kinetic isotopic effect (5 min) values of 1.6, 4.5, and 4.2 were obtained for the **3**-catalyzed dehydrogenation of HCOOD, DCOOH, and DCOOD, respectively, at 353 K. The strong KIE found for DCOOH and DCOOD evidenced that the hydride transfer from the C–H bond of formic acid to the metal is the rate-determining step of the process.
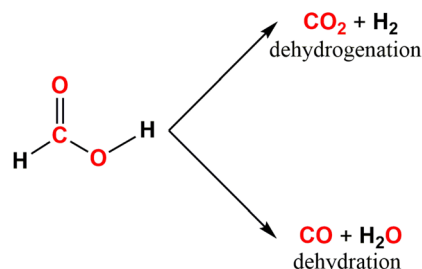
Introduction

The potential of formic acid (FA) as an effective liquid organic hydrogen carrier (LHC) has been the subject of many scientific studies over the past decade.[1] There are many advantages of using FA as LHC, for example, it has a high concentration of H$_2$ (53 g L^{-1}), and it can be easily prepared, stored, and transported.[1] Among its disadvantages it stands out the fact that its dehydrogenation to produce H$_2$ and CO$_2$ competes with its dehydration to give CO and H$_2$O (Scheme 1). Therefore, due to CO poisoning of the Pt electrode in fuel cells,[2] the development of selective catalysts to produce H$_2$ from FA is of great interest to apply FA in fuel cell-based technologies.

To the best of our knowledge, the first studies on the potential of the catalytic formic acid dehydrogenation (FADH) to supply hydrogen to fuel cells were independently reported by Beller *et al.*[3] and Laurenczy *et al.*[4] in 2008. Since then, many examples of catalytic systems active for the FADH have been published.[1,2] The most active catalytic systems for FADH so far reported are based on water soluble Ir–Cp* species with functionalized bipyridine or biimidazoline derivatives as ligands.[5–9] Among them, the species [IrClCp*(2,2′-bi-2-imidazoline)]Cl (TOF ≈ 487 500 h^{-1}),[6] the iridium-bipyridine catalysts described by Fujita and Himeda *et al.* (TOF ≈ 228 000 h^{-1}),[5] and the DMSO soluble Ir–Cp* species reported by Albrecht *el al.* (TOF ≈ 300 000 h^{-1})[10] stand out.

On the other hand, one of the aims of our research group is to study the potential of iridium(III) complexes with pyridine-2-

[a]Departamento de Química Inorgánica – Instituto de Síntesis Química y Catálisis Homogénea (ISQCH). Universidad de Zaragoza. Facultad de Ciencias 50009, Zaragoza, Spain. E-mail: paco@unizar.es
[b]Universidad Pedagógica Nacional Francisco Morazán-UPNFM, 11101 Tegucigalpa, Honduras
†Electronic supplementary information (ESI) available. CCDC 2247182 for compound **3**. For ESI and crystallographic data in CIF or other electronic format see DOI: https://doi.org/10.1039/d3dt00744h

Scheme 1 Possible transformations for FA.

yloxy-silyl ligands (Ir-NSi) as homogenous catalysts.[11–13] These species have been successfully used as CO_2[11] or formamide[12a] hydrosilylation catalysts. Ir-NSi complexes are characterized by their short Ir–Si bond distances (in the range 2.25–2.28 Å),[14] which has been explained by assuming a significant ionic contribution to the covalent bond,[12b,15] and the strong *trans* effect exerted by the silicon atom. Theoretical calculations have shown that the presence of the silicon play a key role in the reactivity of iridium-formate intermediates in catalytic CO_2 hydrosilylation[11] and FADH processes.[16] A challenge when using Ir-NSi complexes as FADH catalysts is that under the reaction conditions the active species can be reduced to inactive iridium nanoparticles.[16] Therefore, with the purpose of preparing iridium(III)-NSi complexes stable under FADH conditions, we decided to use the monoanionic bidentate ligand (4-methylpyridine-2-yloxy)ditertbutylsilyl (NSi^{tBu_2}), where the Ir–Si bond is sterically protected by the bulk of the two *tert*-butyl substituents on the silicon atom.

An additional difficulty when using homogeneous transition metal catalysts with silyl-based ligands in protic solvents is the breaking of the Ir–Si bond, which is favored in the presence of a base.[17] Indeed, the hydrolysis of the Ir–Si bond in Ir-NSi species is favoured in basic-media, moreover the coordination of water to unsaturated Ir-NSi species has been recently reported.[12b] Thus, we decided to explore the potential of electronically and sterically saturated Ir–Si species as FADH catalyst in the absence and in presence of water. In this regard, it should be mentioned that examples of catalytic systems effective for catalytic FADH under neat conditions are scarce.[16,18,19]

Results and discussion

Synthesis of Ir-(NSi^{tBu_2}) complexes with the 4,4′-dimethyl-2,2′-bipyridine ($bipy^{Me_2}$) ligand

Iridium-bipyridine derivatives have shown to be highly effective catalysts in FADH processes.[5] Therefore, to prepare coordinative and electronically saturated Ir-NSi^{tBu_2} species we decided to use 4,4′-dimethyl-2,2′-bipyridine ($bipy^{Me_2}$) as auxiliary bidentate ligand. The reaction of the iridium(III) complex [Ir(H)(Cl)($κ^2$-NSi^{tBu_2})(coe)] (1)[12a] with one equivalent of $bipy^{Me_2}$ at 353 K for 48 h leads to an orange solid, which has been characterized as complex [Ir(H)(Cl)($κ^2$-NSi^{tBu_2})($κ^2$-$bipy^{Me_2}$)] (2) (Scheme 2). The reaction of light protected CH_2Cl_2 solutions of 2 with silver triflate affords a yellow solid of [Ir(H)(OTf)($κ^2$-NSi^{tBu_2})($κ^2$-$bipy^{Me_2}$)] (3) (Scheme 2).

The Ir-($κ^2$-NSi^{tBu_2}) species 2 and 3 have been characterized by means of multinuclear NMR spectroscopy. The ^1H NMR of 2 and 3 in CD_2Cl_2 show a singlet resonance corresponding to the Ir–H at $δ$ −18.03 and −17.53 ppm, respectively. These values are low field shifted with respect to that observed for 1 (−20.68 ppm), 4 (−27.46 ppm) and 5 (−29.21 ppm). The ^1H–^{29}Si HMBC NMR spectra show the resonance due to the silicon atom at $δ$ 46.8 (2) and 41.0 (3), which compare well with the value found for the unsaturated species 1 ($δ$ 41.0),[12a]
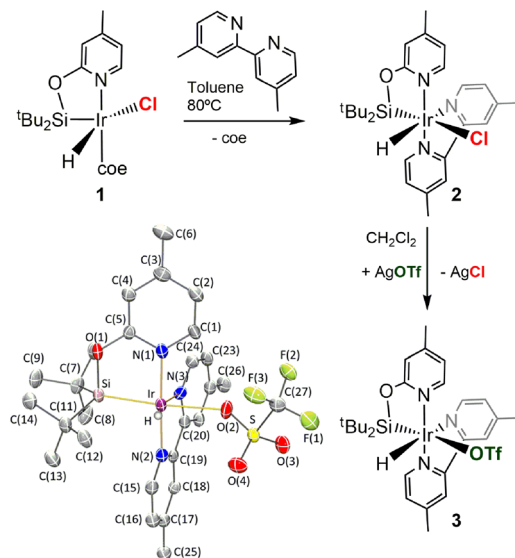
Scheme 2 Preparation of complexes **2** and **3** and molecular structure of complex **3**.

4 ($δ$ 45.8),[12a] and 5 ($δ$ 44.5).[12b] $^{19}F\{^1H\}$ NMR spectra of 3 (at 298 K) in CD_2Cl_2 show a sharp resonance at $δ$ −78.82. Considering that $^{19}F\{^1H\}$ NMR spectra of free TfO⁻ in CD_2Cl_2 (298 K) show a singlet resonance at $δ$ −79.0,[20] the value found for 3 suggests a weak Ir–OTf bond.[12b,20]

In order to attain a deeper understanding about the metal coordination sphere, the solid-state structure of compound 3 has been determined by single crystal X-ray diffraction, using synchrotron radiation. Selected geometrical parameters are reported in Table 1. The metal atom exhibits a distorted octahedral geometry, with a $κ^2$-Si,N and a $κ^2$-N′,N″ coordination of (NSi^{tBu_2}) and $bipy^{Me_2}$, respectively, the hydride and an oxygen atom of the triflate fragment. The Ir–Si and Ir–N(1) bond lengths have been found to be slightly shorter than those reported in compound 1 (2.2853(6) and 2.0947(18) Å, respectively).[12a] Indeed, our previous studies have already revealed that the substitution of the chloride by a triflate ligand (which is a more electron-withdrawing group), reinforce the Ir–Si bond.[12b] On the contrary, the Ir–O(2) bond length in 3 (2.381 (4) Å), with the oxygen *trans* to the silicon, is in the upper limit of Ir–O bond lengths reported in Ir–OTf fragments (in the

Table 1 Selected bonds lengths (Å) and angles (°) found for complex **3**

Ir–Si	2.2731(12)	O(2)–Ir–N(1)	91.53(16)
Ir–O(2)	2.381(4)	O(2)–Ir–N(2)	86.98(16)
Ir–N(1)	2.063(4)	O(2)–Ir–N(3)	75.89(15)
Ir–N(2)	2.044(4)	O(2)–Ir–H	94(3)
Ir–N(3)	2.148(4)	N(1)–Ir–N(2)	175.12(15)
Ir–H	1.53(7)	N(1)–Ir–N(3)	96.75(16)
Si–Ir–O(2)	171.94(13)	N(1)–Ir–H	83(3)
Si–Ir–N(1)	81.92(12)	N(2)–Ir–N(3)	78.38(16)
Si–Ir–N(2)	99.92(12)	N(2)–Ir–H	102(3)
Si–Ir–N(3)	109.42(11)	N(3)–Ir–H	170(3)
Si–Ir–H	81(2)		

2.04–2.40 Å range),[21] indicating a weak bonding, in good agreement with the aforementioned $^{19}F\{^1H\}$ NMR spectra of **3**.

Effect of the ancillary ligand in the performance of Ir-(NSi^{tBu_2}) catalyzed FADH

A comparative study of the activity of complexes **2**, **3**, **4**, and **5** (0.1 mol%) as catalyst precursors for the hydrogen generation from FA-Et$_3$N (40 mol% of Et$_3$N) at 353 K was performed using a man on the moon™ reactor (Fig. 1).[22] It should be mentioned that while compounds **2** and **3** with bipy^{Me_2} as auxiliary bidentate ligand are coordinatively saturated species, complexes **4** [12a] and **5** [12b] are unsaturated species with distorted trigonal bipyramidal and square pyramidal geometries in the solid state, respectively.

The results of these experiments show that complex **3** (TOF$_{5\ min}$ = 1210 h^{-1}) is a more effective catalyst precursor than **2** (TOF$_{5\ min}$ = 900 h^{-1}) (Fig. 2), and both precursors are more active than [Ir(H)(OTf)(κ^2-NSi^{tBu_2})(coe)] (**4**) (TOF$_{5\ min}$ = 600 h^{-1}) and/or [Ir(H)(OTf)(κ^2-NSi^{tBu_2})(PCy$_3$)] (**5**) (TOF$_{5\ min}$ = 60 h^{-1}) (Fig. 2). The systems based on **4** and **5** show the decomposition of the catalyst to give iridium nanoparticles, in a similar fashion to that previously observed for the related Ir-(κ^2-NSi^{Me_2})$_2$ species.[16] Conversely, the formation of iridium nanoparticles was not observed when using **2** or **3**. These results show that the use of coordinatively saturated catalyst

precursors prevents the reduction of iridium(III) and encouraged us to study the performance of **3** as catalyst for FADH.

Subsequently, we have studied the influence of the catalyst loading on the catalytic performance of **3**. The activity of the **3**-catalyzed FADH in presence of Et$_3$N (40 mol%) depends on the catalyst loading, thus using a 0.05 mol%, instead of 0.1 mol%, a reduction of the activity was observed (TOF$_{5\ min}$ = 820 h^{-1}; Fig. S14†). Therefore, we decided to use a 0.1 mol% loading in the following studies.

Once the best catalyst precursor, **3**, was chosen and the catalyst loading (0.1 mol%) optimized, we decided to study the effect of temperature on the performance. Thus, we have studied the catalytic FADH using **3** (0.1 mol%) as catalyst precursor in the presence of an initial concentration of Et$_3$N of 40 mol% at different temperatures (Fig. 3). These studies revealed that, as expected, the temperature produces a positive effect on the activity of the reaction (Fig. 3) and allowed us to determinate the initial reaction rates (TOF$_{5\ min}$) at 323, 333, 343, 353, 363 and 373 K (Table S16†). The Arrhenius plot for these data[23] yields an apparent activation energy of 16.76 ± 1.72 kcal mol^{-1}, which is lower than that found for the related [Ir(CF$_3$CO$_2$)(κ^2-NSi^{Me_2})$_2$] species (27.5 kcal mol^{-1})[16] and agrees with the greater activity of **3** in comparison to that found for [Ir(CF$_3$CO$_2$)(κ^2-NSi^{Me_2})$_2$], under the same reaction conditions (Table 2).

The activity of the catalytic system **3**/Et$_3$N (40 mol%) as FADH catalyst (373 K; TOF$_{5\ min}$ = 3260 h^{-1}) is higher than that reported for the iridium(III) complexes [Ir(CF$_3$CO$_2$)(κ^2-NSi^{Me_2})$_2$] (373 K; TOF$_{5\ min}$ = 2900 h^{-1})[16] and [Ir(COD)(NP^{tBu})][TfO] (363 K; TOF$_{5\ min}$ = 3000 h^{-1})[18] but lower than that reported for the manganese compound [Mn(CO)$_2$(^{tBu}PNNOP)] (353 K; TOF$_{5\ min}$ = 8500 h^{-1})[24] (Table 2) and for the iridium(III) species reported by Fischmeister *et al.* (TOF ≈ 13 300 h^{-1}),[19a] Iglesias *et al.* (TOF ≈ 11 600 h^{-1})[19b] and Gelman *et al.* (TOF ≈ 11 800 h^{-1}).[19c]

FTIR studies of the gases resulting from these **3**-catalyzed reactions evidenced that the selectivity of the catalytic process
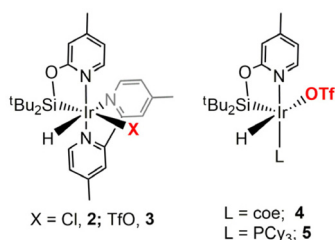

Fig. 1 Ir-(NSi^{tBu_2}) catalyst precursors.
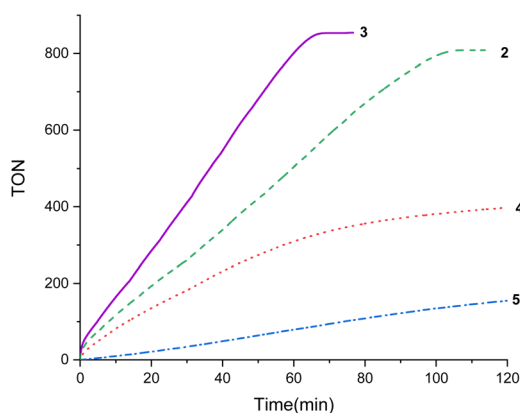

Fig. 2 TON *versus* time (min) from the **2**, **3**, **4** or **5** catalyzed (0.1 mol%) solventless dehydrogenation of FA-Et$_3$N adduct (Et$_3$N 40 mol%) at 353 K. The gas evolution was measured using a man on the moon™ reactor[22] (H$_2$: CO$_2$ = 1 : 1).
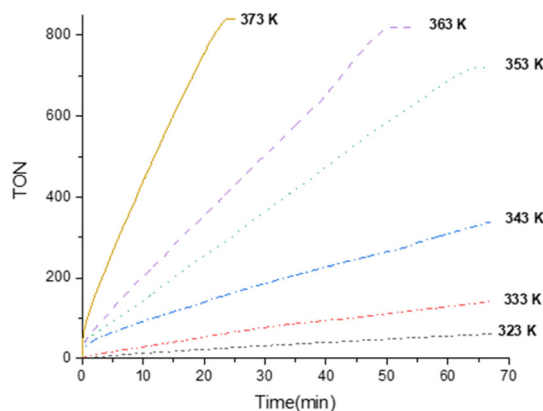

Fig. 3 TON *versus* time (min) from the **3**-catalyzed (0.1 mol%) solventless dehydrogenation of FA-Et$_3$N adduct (Et$_3$N 40 mol%) at different temperatures. The gas evolution was measured using a man on the moon™ reactor[22] (H$_2$: CO$_2$ = 1 : 1).

Table 2 Comparison of the activity of **3** (0.1 mol%) as catalyst precursor for the solventless dehydrogenation of FA in presence of the FA–Et$_3$N (5 : 2) adduct or sodium formate with **2**, **4**, **5** and other metal-based catalysts

Catalyst	T (K)	TOF (h^{-1})/(time)	Ref.
4	353	600/(5 min)	This work
5	353	60/(5 min)	This work
2	353	900/(5 min)	This work
3	353	1210/(5 min)	This work
3	373	3260/(5 min)	This work
[Ir(CF$_3$CO$_2$)(κ^2-NSi^{Me_2})$_2$]	373	2900/(5 min)	16
[Ir(CF$_3$CO$_2$)(κ^2-NSi^{Me_2})$_2$]	353	600/(5 min)	16
[Mn(CO)$_2$(^{tBu}PNNOP)]	353	8500/(3 min)	24
[RuCl$_2$(PPh$_3$)$_3$]	313	400/(2 h)	3
[Ir(COD)(NP^{tBu})][TfO] ^{a}	363	3000 ^{b}	18

^{a} sodium formate instead FA-Et$_3$N (5 : 2) adduct, ^{b} Maximum Turnover Frequency.

depends on the temperature. Thus, while at 353 K, the formation of CO was below the detection limit of the FTIR (3 ppm) and, therefore, the selective formation of H$_2$ and CO$_2$ and residual Et$_3$N was observed (Fig. 4), the FTIR spectra of the gases obtained from the reactions at 373 K shows the presence of traces of CO (Fig. S17†). It is known that the dehydration of neat FA to form H$_2$O and CO is favored at high temperatures.[25] Therefore, it is reasonable to assume that the traces of CO observed at 373 K may be formed by thermal, uncatalyzed decomposition pathways.[26]

Kinetic isotope experiments on the **3**-catalyzed FADH were performed at 353 K using 40 mol% of Et$_3$N (Table 3 and Fig. 5). The results from these studies show that the initial TOF values (calculated after 5 min) dropped from 1210 to 770, 270 and 290 h^{-1} when HCOOH was replaced by HCOOD, DCOOH and DCOOD, respectively (Table 3). These TOF$_{5 min}$ values show a high kinetic isotopic effect (KIE) for DCOOH and DCOOD of 4.5 and 4.2, respectively (Table 3, entries 3 and 4), which evidenced that the hydride transfer from the CH of FA to the metal leading to CO$_2$ is the rate-determining step of

Fig. 4 FTIR of the gas resulting from the solventless **3**-catalyzed (0.1 mol%) FADH in presence of Et$_3$N at 353 K.

Table 3 Kinetic isotope effect experiments on the **3**-catalyzed dehydrogenation of FA using 40 mol% of Et$_3$N at 353 K

Entry	Substrate	TOF$_{5 min}$ ^{a}/(KIE) ^{b}
1	HCOOH	1210/(—)
2	HCOOD	770/(1.6)
3	DCOOH	270/(4.5)
4	DCOOD	290/(4.2)

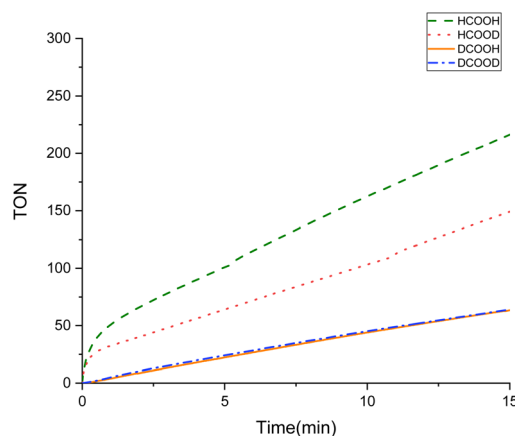^{a} h^{-1}; ^{b} KIE = entry 1 / the corresponding entry (**2**, **3** or **4**).

Fig. 5 TON *versus* time (min) from the **3**-catalyzed (0.1 mol%) solventless dehydrogenation of HCOOH, HCOOD, DCOOH and DCOOD in presence of Et$_3$N 40 mol% at 353 K. The gas evolution was measured using a man on the moon™ reactor.[22]

the process.[26] Moreover, the KIE value (1.6) obtained when using HCOOD show a secondary KIE effect, analogous to that found for the related Ir-(κ^2-NSi^{Me_2})$_2$ species (Table 3, entry 2).[16]

In all the studied **3**-catalyzed (0.1 mol%) dehydrogenation of FA-Et$_3$N (Et$_3$N 40 mol%) reactions, once the gas evolution ends a blue residue remains in the reactor. ^{1}H NMR spectra (DMSO-d$_6$) of these blue residues show the presence of triethylammonium salts, a major component of the mixture, together with several unidentified Ir–H species. ^{1}H–^{29}Si HMBC spectra shows three different silicon resonances (Fig. S19†). Two of them correspond to compounds with ^{t}Bu$_2$Si groups not bonded to Ir (^{29}Si{^{1}H} NMR; δ −14.11 and −22.85 ppm), but the remaining resonance is due to a complex with an Ir–Si bond (^{29}Si{^{1}H} NMR; δ 45.11) and two inequivalent ^{t}Bu substituents (Fig. 6).

The addition of a second load of FA (50 μL) to this blue residue at 353 K evidenced that it catalyzed FADH. However, a decrease of the activity (TOF$_{5 min}$ ≈ 940 h^{-1}) was observed (Fig. 7). This demonstrates that, although the use of 4,4′-dimethylbipyridine as ancillary ligand somehow protects the Ir–Si bond, the partial deactivation of the active species still occurs. It should be mentioned that the blue-residue is still active after 24 h (TOF$_{5 min}$ ≈ 270 h^{-1}) (Fig. S15†).

Therefore, the catalytic system based on **3**, with bipy^{Me_2} as auxiliary ligand, is more active (Table 2) and stable than [Ir(CF$_3$CO$_2$)(κ^2-NSi^{Me_2})$_2$].[16] This encouraged us to study its per-
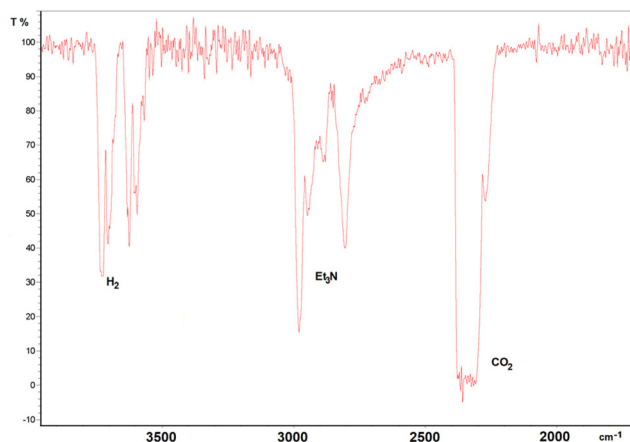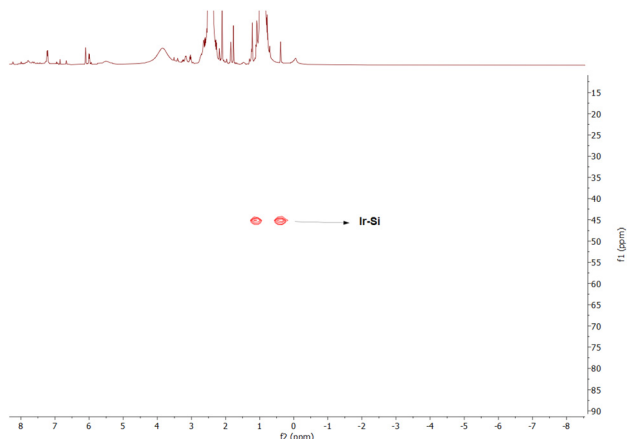
Fig. 6 ^{1}H–^{29}Si HMBC spectrum DMSO-d$_6$ (400 MHz, 298 K) of the blue residue from the solventless **3**-catalyzed (0.1 mol%) FADH in presence of Et$_3$N (40 mol%) at 353 K.
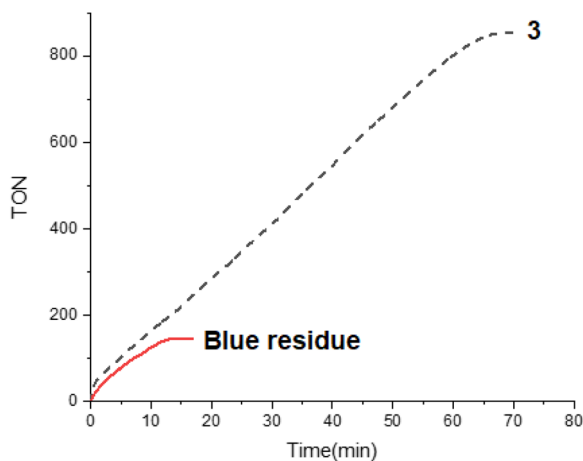

Fig. 7 TON *versus* time (min) from the **3**-catalyzed (0.1 mol%) of FA (250 µL) in presence of Et$_3$N 40 mol% or the blue-residue catalyzed solventless dehydrogenation of HCOOH (50 µL) at 353 K. The gas evolution was measured using a man on the moon™ reactor.[22]

Fig. 8 TON *versus* time (min) from the solventless **3**-catalyzed (0.1 mol%) of FA (250 µL) in presence of Et$_3$N 40 mol% (blue) at 353 K or **3**-catalyzed (0.1 mol%) of FA (250 µL)/H$_2$O (250 µL) in presence of Et$_3$N 40 mol% at 353 K. The gas evolution was measured using a man on the moon™ reactor.[22]

All reactions and manipulations were carried out under an argon atmosphere by using Schlenk-type techniques or in a Glovebox-MBraun UNIlab. Organic solvents were dried by standard procedures and distilled under argon prior to use or obtained oxygen- and water-free from a Solvent Purification System (Innovative Technologies). ^{1}H, ^{13}C, ^{29}Si, ^{31}P and ^{19}F NMR spectra were obtained on a Bruker AV-300, AV-400 or AV-500 spectrometer using TMS as the internal reference in CD$_2$Cl$_2$, or DMSO-d$_6$ as solvent. All chemical shifts (δ) are reported in ppm and coupling constants (J) are reported in Hz to apparent peak multiplets. ^{1}H–^{1}H-COSY, ^{13}C-APT, ^{1}H/^{13}C HSQC, ^{1}H/^{13}C HMBC and ^{1}H/^{29}Si HMBC sequences were used for help in the assignments of the ^{1}H, and ^{13}C{^{1}H} spectra. All catalytic experiments have been reproduced a minimum of three times.

Synthesis of [Ir(H)(Cl)(κ^2-NSi^{tBu_2})(κ^2-bipy^{Me_2})] (2)

Toluene (10 mL) was added to a mixture of [Ir(Cl)(H)(κ^2-NSi^{tBu_2})(coe)] (**1**) (0.538 g, 0.913 mmol) and 4,4′-dimethyl-bypyridine (0.185 g, 1.004 mmol). The reaction mixture was warmed at 353 K and stirred for 48 hours to give a dark-red solution and an orange precipitate. After that, the reaction mixture was cooled to 273 K. The red solution was filtered through Celite and the residue was washed with hexane (2 × 5 mL) and CH$_2$Cl$_2$ (2 × 2 mL) to give an orange solid of **2**. 425 mg (70%). Anal. calcd for C$_{26}$H$_{37}$ClIrN$_3$OSi: C, 47.08; H, 5.62; N, 6.33, found C, 46.93; H, 5.68; N, 6.48. ^{1}H NMR plus COSY (300 MHz, CD$_2$Cl$_2$, 298 K): δ 9.33 (d, $^3J_{H-H}$ = 6.3 Hz, 1H, H^6–Py), 9.18 (d, $^3J_{H-H}$ = 6.0 Hz, 1H, H^6–Bpy), 7.96 (s, 1H, H^3–Bpy), 7.91 (d, $^3J_{H-H}$ = 5.6 Hz, 1H, H^6–Bpy), 7.87 (s, 1H, H^3–Bpy), 7.20 (d, $^3J_{H-H}$ = 5.6 Hz, 1H, H^5–Bpy), 7.02 (d, $^3J_{H-H}$ = 6.0 Hz, H^5–Bpy), 6.69 (s, 1H, H^3–Py), 6.58 (d, $^3J_{H-H}$ = 6.5 Hz, 1H, H^5–Py), 2.48 (s, 3H, Me–Bpy), 2.44 (s, 3H, Me–Bpy), 2.32 (s, 3H, Me–Py), 1.09 (s, 9H, tBu–Si), 0.44 (s, 9H, tBu–Si), −18.03 (s, 1H, Ir–H). ^{13}C{^{1}H} NMR APT plus HSQC, COSY and NOESY (75 MHz, CD$_2$Cl$_2$, 298K): δ 158.7 (C^6–Bpy), 151.2 (C$_{ipso}$), 150.7

formance as FADH catalyst in an aqueous medium. These studies show that initially the system based on **3** (0.1 mol%), in presence of Et$_3$N (40 mol%) at 353 K, is slightly more active in water solution (TOF$_{5\ min}$ = 1500 h^{-1}) than under solventless conditions. However, after 15 min of reaction catalyst deactivation is observed (Fig. 8).

Experimental

General information

Complexes **1**,[12a] **4**,[12a] and **5**[12b] were prepared according to the reported method. HCOOH, HCOOD, DCOOH and DCOOD were purchased from commercial sources and used without further purifications. Et$_3$N was purchased from commercial sources and distilled prior to use.
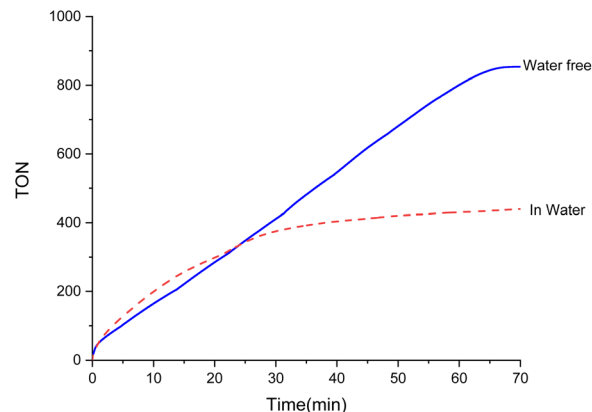
(C^6–Py), 150.7 (C^6–Bpy), 149.2 (C_{ipso}), 147.8 (C_{ipso}), 147.7 (C^6–Bpy), 128.0 (C^5–Bpy), 127.4 (C^5–Bpy), 124.3 (C^3–Bpy), 124.0 (C^3–Bpy), 117.9 (C^5–Py), 111.0 (C^3–Py), 29.9 (CMe_3), 29.0 (CMe_3), 25.6 (CMe_3), 25.3 (CMe_3), 21.9 (Me–Bpy), 21.7 (Me–Bpy), 21.20 (Me–Py). ^{1}H–^{29}Si HMBC (60 MHz, CD_2Cl_2, 298 K): δ 46.8. High-resolution mass spectrometry (ESI+): calcd m/z = 663.2024; found m/z = 628.2339 (M ± Cl).

Synthesis of [Ir(H)(OTf)(κ^2-NSi^{tBu_2})(κ^2-bipy^{Me_2})] (3)

CH_2Cl_2 (8 mL) was added to a mixture of complex **2** (0.370 g, 0.558 mmol) and silver triflate (0.157 g, 0.614 mmol). The resulting suspension was stirred overnight at room temperature. The orange solution was filtered through Celite and the solvent was removed *in vacuo*, washed with hexane (2 × 5 mL) and dried *in vacuo* to give a yellow powder of **3**.320 mg (74%). Anal. calcd for $C_{27}H_{37}F_3IrN_3O_4SSi$: C, 41.74; H, 4.80; N, 5.41; S, 4.13; found C, 41.23; H, 4.78; N, 5.18; S, 4.36. ^{1}H NMR plus COSY (300 MHz, CD_2Cl_2, 298 K): δ 9.08 (d, $^3J_{H–H}$ = 5.9 Hz, 1H, H^6–Bpy), 8.43 (d, $^3J_{H–H}$ = 6.2 Hz, 1H, H^6–Py), 8.02 (s, 1H, H^3–Bpy), 7.94 (s, 1H, H^3–Bpy), 7.82 (m, 1H, H^6–Bpy), 7.32 (m, 1H, H^5–Bpy), 7.10 (m, 1H, H^5–Bpy), 6.76 (m, 1H, H^3–Py), 6.71 (m, 1H, H^5–Py), 2.52 (s, 3H, Me–Bpy), 2.47 (s, 3H, Me–Bpy), 2.36 (s, 3H, Me–Py), 1.07 (s, 9H, tBu-Si), 0.47 (s, 9H, tBu-Si), −17.40 (br, 1H, Ir–H). ^{13}C{^{1}H} NMR APT plus ^{1}H–^{13}C HSQC: δ 169.3 (C_{ipso}), 159.9 (C^6–Bpy), δ 159.1 (C_{ipso}), 158.0 (C_{ipso}), 148.3 (C^6–Py), 147.7 (C^6–Bpy), 128.5 (C^5–Bpy), 127.8 (C^5–Bpy), 124.4 (C^3–Bpy), 124.2 (C^3–Bpy), 118.9 (C^5–Py), 111.7 (C^3–Py), 29.7 (CMe_3), 28.8 (CMe_3), 25.4 (CMe_3), δ 24.3 (CMe_3), 22.2 (Me–Bpy), 22.0 (Me–Bpy), 21.4 (Me–Py). ^{1}H–^{29}Si HMBC (60 MHz, CD_2Cl_2, 298 K): δ 41.0. ^{19}F{^{1}H} NMR (300 MHz, CD_2Cl_2, 298 K): δ −78.82 (s, Ir–OTf). High-resolution mass spectrometry (ESI+): calcd m/z = 777.1855; found m/z = 628.2339 (M ± OTf).

Single crystal structure determination of 3

X-ray data of **3** were collected in the XALOC beamline at ALBA synchrotron (Spain).[27] Data were collected at 100 K with 0.72940 Å wavelength, using the Dectris Pilatus 6 M detector placed at 122.1 mm from the crystal. The complete φ scans were performed in steps of 0.5°, with an exposure time of 0.1 s per frame. Intensity transmission was attenuated to 20%. Sample crystallized as weakly diffracting thin needles, which suffered radiation damage during data collection. Several crystals were measured and subsequently merged. However, this strategy led to worst agreement factors. Therefore, the best data set was selected to perform the structural refinement. Small redundancy in the measured diffraction of this anisotropic sample may affect the absorption correction process. Data were indexed, integrated, and scaled using APEX4 package.[28] The crystal structure was solved and refined using SHELXS[29] and SHELXL[30] in OLEX2 program.[31]

Crystal data of 3. $C_{27}H_{37}F_3IrN_3O_4SSi·C_7H_8$; M_r = 3661.7(2); yellow needle 0.005 × 0.020 × 0.060 mm^3; monoclinic $P2_1/c$; a = 15.8989(6) Å, b = 19.4839(7) Å; c = 11.8251(4) Å, β = 91.561(2)°; V = 3661.7(2) Å^3; Z = 4; D_c = 1.576 g cm^{-3}; μ = 4.032 mm^{-1}; min. and max. absorption correction factors: 0.1248 and 0.2709; $2\theta_{max}$ = 68.182°; 53 433 reflections measured, 11 179

unique; R_{int} = 0.0781; number of data/restraint/parameters: 11 179/0/438; $R1$ = 0.0595 [9705 reflections, $I > 2\sigma(I)$], w$R(F^2)$ = 0.1756 (all data); largest difference peak: 6.91 e Å^{-3}. Highest residual density peaks are found close to the metal atom.

General procedure for the formic acid dehydrogenation under neat conditions

Catalytic reactions were carried out on a microreactor (man on the moon™ series X102 Kit)[22] with a total volume of 16.2 mL. Under an argon atmosphere, the reactor was filled with 250 μL of formic acid and the corresponding amount of the catalyst precursor. The reactor was then closed and heated to the desired temperature in an oil bath, and when the temperature and pressure of the system are stabilized, Et_3N (370 μL, 40 mol% to FA) is injected with a microsyringe.

Procedure for the formic acid dehydrogenation in water

Catalytic reactions were carried out on a microreactor (man on the moon™ series X102 Kit)[22] with a total volume of 16.2 mL. Under an argon atmosphere, the reactor was filled with 250 μL of formic acid, 250 μL of distilled water, and the corresponding amount of the catalyst precursor. The reactor was then closed and heated to the desired temperature in an oil bath, and when the temperature and pressure of the system are stabilized, Et_3N (370 μL, 40 mol% to FA) is injected with a microsyringe.

Conclusions

The iridium(III) complexes **2**, **3**, **4** and **5** (0.1 mol%) are effective catalyst precursors for the solventless FADH in presence of Et_3N (40 mol%). The catalytic system based on **3** has proven to be the most active of them all. The best catalytic performance (activity/selectivity) was achieved using **3** at 353 K (TOF$_5$ $_{min}$ ≈ 1210 h^{-1}). The highest activity (TOF$_5$ $_{min}$ ≈ 3260 h^{-1}) has been obtained with **3** at 373 K. However, at that temperature the FTIR spectra of the resulting gas show that the desired products (H_2 and CO_2) are impurified by traces of CO.

Kinetic studies at variable temperature show that the activation energy of the **3**-catalyzed FADH process is 16.76 kcal mol^{-1}. KIE values of 1.6, 4.5, and 4.2 were obtained for the **3**-catalyzed dehydrogenation of HCOOD, DCOOH, and DCOOD, respectively, at 353 K. The strong KIE found for DCOOH, and DCOOD (>4.0) evidenced that the activation of the C–H bond of FA is the rate-determining step of the process.

In conclusion, the use of the ligand κ^2-NSi^{tBu_2} with two *tert*-butyl substituents on the silicon atom and 4,4′-dimethyl-bipyridine as ancillary ligand enhances the catalytic performance of Ir-NSi species as FADH catalyst precursors under solventless conditions. However, their use in an aqueous medium is hampered due to the short life of the catalyst under these conditions.

Conflicts of interest

There are no conflicts to declare.

Acknowledgements

References

1 For recent reviews see: (*a*) M. Iglesias and F. J. Fernández-Alvarez, *Catalysts*, 2021, **11**, 1288, DOI: 10.3390/catal11111288; (*b*) K. Grubel, H. Jeong, C. W. Yoon and T. Autrey, *J. Energy Chem.*, 2020, **41**, 216–224; (*c*) C. Guan, Y. Pan, T. Zhang, M. J. Ajitha and K.-W. Huang, *Chem. – Asian J.*, 2020, **15**, 937–946; (*d*) P. Stathi, M. Solakidou, M. Louloudi and Y. Deligiannakis, *Energies*, 2020, **13**, 733; (*e*) M. Iglesias and L. A. Oro, *Eur. J. Inorg. Chem.*, 2018, 2125–2138; (*f*) K. Sordakis, C. Tang, L. K. Vogt, H. Junge, P. J. Dyson, M. Beller and G. Laurenczy, *Chem. Rev.*, 2018, **118**, 372–433; (*g*) N. Onishi, G. Laurenczy, M. Beller and Y. Himeda, *Coord. Chem. Rev.*, 2018, **373**, 317–332; (*h*) P. Preuster, C. Papp and P. Wasserscheid, *Acc. Chem. Res.*, 2017, **50**, 74–85; (*i*) J. Eppinger and K.-W. Huang, *ACS Energy Lett.*, 2017, **2**, 188–195; (*j*) D. Mellmann, P. Sponholz, H. Junge and M. Beller, *Chem. Soc. Rev.*, 2016, **45**, 3954–3988; (*k*) A. K. Singh, S. Singh and A. Kumar, *Catal. Sci. Technol.*, 2016, **6**, 12–40.

2 (*a*) G. Kim and S.-H. Jhi, *ACS Nano*, 2011, **5**, 805–810; (*b*) S. K. Das, A. Reis and K. J. Berry, *J. Power Sources*, 2009, **193**, 691–698; (*c*) J. J. Baschuk and X. Li, *Int. J. Energy Res.*, 2001, **25**, 695–713.

3 B. Loges, A. Boddien, H. Junge and M. Beller, *Angew. Chem., Int. Ed.*, 2008, **47**, 3962–3965.

4 C. Fellay, P. J. Dyson and G. Laurenczy, *Angew. Chem., Int. Ed.*, 2008, **47**, 3966–3968.

5 J. F. Hull, Y. Himeda, W.-H. Wang, B. Hashiguchi, R. Periana, D. J. Szalda, J. T. Muckerman and E. Fujita, *Nat. Chem.*, 2012, **4**, 383–388.

6 Z. Wang, S.-M. Lu, J. Li, J. Wang and C. Li, *Chem. – Eur. J.*, 2015, **21**, 12592–12595.

7 Y. Himeda, *Green Chem.*, 2009, **11**, 2018–2022.

8 A. Matsunami, Y. Kayaki and T. Ikariya, *Chem. – Eur. J.*, 2015, **21**, 13513–13517.

9 A. Matsunami, S. Kuwata and Y. Kayaki, *ACS Catal.*, 2017, **7**, 4479–4484.

10 N. Lentz and M. Albrecht, *ACS Catal.*, 2022, **12**, 12627–12631.

11 (*a*) J. Guzmán, P. García-Orduña, V. Polo, F. J. Lahoz, L. A. Oro and F. J. Fernández-Alvarez, *Catal. Sci. Technol.*, 2019, **9**, 2858–2867; (*b*) J. Guzmán, P. García-Orduña, F. J. Lahoz and F. J. Fernández-Alvarez, *RSC Adv.*, 2020, **10**, 9582–9586; (*c*) J. Guzmán, A. Urriolabeitia, M. Padilla, P. García-Orduña, V. Polo and F. J. Fernández-Alvarez, *Inorg. Chem.*, 2022, **61**(50), 20216–20221.

12 (*a*) J. Guzmán, A. M. Bernal, P. García-Orduña, F. J. Lahoz, L. A. Oro and F. J. Fernández-Alvarez, *Dalton Trans.*, 2019, **48**, 4255–4262; (*b*) A. Gómez-España, P. García-Orduña, J. Guzmán, I. Fernández and F. J. Fernández-Alvarez, *Inorg. Chem.*, 2022, **61**, 16282–16294.

13 F. J. Fernández-Alvarez, R. Lalrempuia and L. A. Oro, *Coord. Chem. Rev.*, 2017, **350**, 49–60.

14 J. Guzmán, A. M. Bernal, P. García-Orduña, F. J. Lahoz, V. Polo and F. J. Fernández-Alvarez, *Dalton Trans.*, 2020, **49**, 17665–17673.

15 For related studies see: P. García-Orduña, I. Fernández, L. A. Oro and F. J. Fernández-Alvarez, *Dalton Trans.*, 2021, **50**, 5951–5959.

16 J. Guzmán, A. Urriolabeitia, V. Polo, M. Fernández-Buenestado, M. Iglesias and F. J. Fernández-Alvarez, *Dalton Trans.*, 2022, **51**, 4386–4393.

17 L. Turculet, PSiP Transition-Metal Pincer Complexes: Synthesis, Bond Activation, and Catalysis, Chapter 6, in *Pincer and Pincer-Type Complexes: Applications in Organic Synthesis and Catalysis*, ed. K. J. Szabó and O. F. Wendt, John Willey and Sons, 1st edn, 2014.

18 J. J. A. Celaje, Z. Lu, E. A. Kedzie, N. J. Terrile, J. N. Lo and T. J. Williams, *Nat. Commun.*, 2016, **7**, 11308.

19 (*a*) S. Wang, H. Huang, T. Roisnel, C. Bruneau and C. Fischmeister, *ChemSusChem*, 2019, **12**, 179–184; (*b*) A. Iturmendi, M. Iglesias, J. Munarriz, V. Polo, V. Passarelli, J. J. Pérez-Torrente and L. A. Oro, *Green Chem.*, 2018, **20**, 4875–4879; (*c*) S. Cohen, V. Borin, I. Schapiro, S. Musa, S. De-Botton, N. V. Belkova and D. Gelman, *ACS Catal.*, 2017, **7**, 8139–8146; (*d*) A. Luque-Gómez, S. García-Abellán, J. Munarriz, V. Polo, V. Passarelli and M. Iglesias, *Inorg. Chem.*, 2021, **60**, 15497–15508.

20 E. Suárez, P. Plou, D. G. Gusev, M. Martín and E. Sola, *Inorg. Chem.*, 2017, **56**, 7190–7199.

21 (*a*) Cambridge Structural Database. CSD version 5.43 update Nov 2022; ; (*b*) C. R. Groom, I. J. Bruno, M. P. Lightfoot and S. C. Ward, *Acta Crystallogr., Sect. B: Struct. Sci., Cryst. Eng. Mater.*, 2016, **72**, 171–179.

22 https://www.manonthemoontech.com/.

23 For recent examples of catalytic FADH activation parameters obtained from Arrhenius plot using initial TOF values see: (*a*) M. Iguchi, H. Zhong, Y. Himeda and H. Kawanami, *Chem. – Eur. J.*, 2017, **23**, 17017–17021; (*b*) Y. Manaka, W.-H. Wang, Y. Suna, H. Kambayashi, J. T. Muckerman, E. Fujita and Y. Himeda, *Catal. Sci. Technol.*, 2014, **4**, 34–37; (*c*) H. Junge, M. Beller and

H. Grützmacher, *ChemSusChem*, 2018, **11**, 3092–3095; (*d*) W.-H. Wang, H. Wang, Y. Yang, X. Lai, Y. Li, J. Wang, Y. Himeda and M. Bao, *ChemSusChem*, 2020, **13**, 5015–5022.

24 N. H. Anderson, J. Boncella and A. M. Tondreau, *Chem. – Eur. J.*, 2019, **25**, 10557–10560.

25 (*a*) J. Yu and P. E. Savage, *Ind. Eng. Chem. Res.*, 1998, **37**, 2–10; (*b*) N. Akiya and P. E. Savage, *AIChE J.*, 1998, **44**, 405–415.

26 G. Menendez Rodriguez, F. Zaccaria, L. Tensi, C. Zuccaccia, P. Belanzoni and A. Macchioni, *Chem. – Eur. J.*, 2021, **27**, 2050–2064.

27 J. Juinhuix, F. Gil-Ortiz, G. Cuní, C. Colldelram, J. Nicolás, J. Lidón, E. Boter, C. Ruget, S. Ferrer and J. Benach, *J. Synchrotron Radiat.*, 2014, **21**, 679–686.

28 G. M. Sheldrick, *Acta Crystallogr., Sect. A: Found. Crystallogr.*, 2008, **64**, 112–122.

29 G. M. Sheldrick, *Acta Crystallogr., Sect. C: Struct. Chem.*, 2015, **871**, 3–8.

30 *APEX 4 v2021.10-0. Bruker AXS*.

31 O. V. Dolomanov, L. J. Bourhus, R. J. Gildea, J. A. K. Howard and H. Puschmann, *J. Appl. Crystallogr.*, 2009, **42**, 339–341.